Spontaneous conformational change and toxin binding in α7 acetylcholine receptor: Insight into channel activation and inhibition

Myunggi Yi, Harianto Tjong, and Huan-Xiang Zhou*

Department of Physics and Institute of Molecular Biophysics and School of Computational Science, Florida State University, Tallahassee, FL 32306

Edited by Robert M. Stroud, University of California, San Francisco, CA, and approved April 11, 2008 (received for review November 5, 2007)

Nicotinic AChRs (nAChRs) represent a paradigm for ligand-gated ion channels. Despite intensive studies over many years, our understanding of the mechanisms of activation and inhibition for nAChRs is still incomplete. Here, we present molecular dynamics (MD) simulations of the α7 nAChR ligand-binding domain, both in apo form and in α-Cobratoxin-bound form, starting from the respective homology models built on crystal structures of the acetylcholine-binding protein. The toxin-bound form was relatively stable, and its structure was validated by calculating mutational effects on the toxin-binding affinity. However, in the apo form, one subunit spontaneously moved away from the conformation of the other four subunits. This motion resembles what has been proposed for leading to channel opening. At the top, the C loop and the adjacent β7-β8 loop swing downward and inward, whereas at the bottom, the F loop and the C terminus of β10 swing in the opposite direction. These swings appear to tilt the whole subunit clockwise. The resulting changes in solvent accessibility show strong correlation with experimental results by the substituted cysteine accessibility method upon addition of acetylcholine. Our MD simulation results suggest a mechanistic model in which the apo form, although predominantly sampling the ''closed'' state, can make excursions into the ''open'' state. The open state has high affinity for agonists, leading to channel activation, whereas the closed state upon distortion has high affinity for antagonists, leading to inhibition.

allostery | spontaneous opening | ligand-gated ion channel | ligand binding

Nicotinic AChRs (nAChRs) are a well studied prototype for ligand-gated ion channels (1–19). nAChRs are pentamers consisting of either homo or hetero subunits. The N-terminal extracellular regions of the subunits make up the ligand-binding domain (LBD), with two or five binding sites in hetero and homo pentamers, respectively. The central regions form the transmembrane domain (TMD), which is an ion channel selective for cations such as Na^+, K^+, and Ca^{2+} [supporting information (SI) Fig. S1]. A central issue is the mechanisms of channel activation by agonists and inhibition by antagonists. How is agonist/antagonist binding transmitted to trigger channel opening/closing? What are the necessary conformational changes? Experimental and computational studies together have begun to provide mechanistic insights at the atomic level. Here, we present a molecular dynamics (MD) simulation study of the α7 nAChR LBD (consisting of five α-type subunits), both in apo form and in α-Cobratoxin-bound form. Our simulation results are in broad agreement with a wealth of experimental data. Combining the present work with experimental data and previous computational results, we propose a mechanistic model in which the apo form, although predominantly sampling the ''closed'' state, can make excursions into the ''open'' state. Details of the conformational change leading to channel activation/inhibition are presented.

A number of structural models for the conformational changes leading to channel activation have been proposed. In the model proposed by Unwin (15), the inner β sheet of the extracellular region of each subunit rotates clockwise relative to the outer β sheet (top view in Fig. S1*A*); the inner β sheet is assumed to be coupled to the TMD, and hence when the former rotates, the latter is dragged along, leading to channel opening. However, the proposed relative rotation between the two β sheets is not seen in MD simulations (9, 13) and does not appear to be consistent with acetylcholine-induced changes in residue solvent accessibilities measured by the substituted cysteine accessibility method (SCAM) (10, 19).

From normal mode analysis, Changeux, Karplus, and coworkers (14, 18) proposed the lowest-frequency mode as the model for channel activation. In this ''quaternary twist'' model, the LBD rotates counterclockwise around the central axis, and the TMD rotates in the opposite direction (top view). This motion was also found to be the first mode in a normal mode analysis of McCammon and coworkers (16), but the latter authors built a structural model for channel activation by linearly combining the first and second modes. The resulting model appears to reproduce some aspects of the Unwin model. McCammon and coworkers (17) also carried out targeted MD simulations, in which the C loop is pulled from the ''up'' to the ''down'' position (side view in Fig. S1*B*); the latter position is observed when an agonist is bound (20). This downward motion of the C loop triggers the motion of the tip of the F loop, the C terminus of β10, and the β1-β2 loop in the opposite direction. The latter motion is coupled to rotation of the TMD, which in turn is assumed to lead to channel opening.

Our study is based on MD simulations in explicit solvent. The toxin-bound form is found to be relatively stable, and the structure of the LBD–toxin complex is validated by comparing calculated mutational effects on the binding affinity against experimental data (8). In the apo form, one subunit spontaneously moves away from the ''closed'' conformation of the other subunits, with motions resembling those obtained in targeted MD simulations (17). We propose that this subunit has undergone a transition from the closed to the open conformation, whereas the other four subunits remain in the closed conformation. The details of our open conformation correlate well with the SCAM results of Rosenberg and coworkers (10, 19). In particular, relative to the closed conformation, both our MD simulations and SCAM find that residues M37 and M40 in the β1 strand have decreased solvent accessibility, whereas N52 in β2 has increased solvent accessibility. The F loop residues N170 and E172 also show opposite changes in solvent accessibility.

Author contributions: H.-X.Z. designed research; M.Y. and H.T. performed research; M.Y. analyzed data; and M.Y. and H.-X.Z. wrote the paper.

The authors declare no conflict of interest.

This article is a PNAS Direct Submission.

*To whom correspondence should be addressed. E-mail: zhou@sb.fsu.edu.

This article contains supporting information online at www.pnas.org/cgi/content/full/0710530105/DCSupplemental.

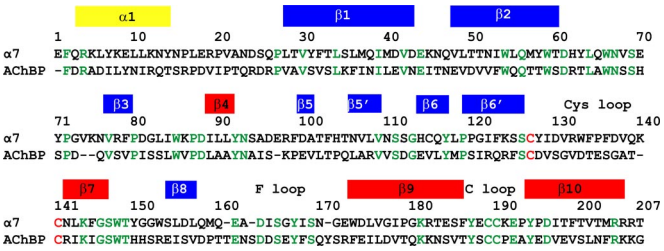

Fig. 1. Sequence alignment between *G. gallus* α7 receptor LBD and *L. stagnalis* AChBP. α7 residue numbering is shown. Identical residues are colored in green. α helix and β strands in inner and outer sheets are indicated by yellow, blue, and red bars, respectively.

Results and Discussion

Homology Model, Conformational Distortions, and Flexibility. The apo and α-Cobratoxin-bound forms of chicken α7 LBD were built by homology on the structures of the respective forms of the acetylcholine-binding protein (AChBP) (21, 22). The sequence alignment between the α7 N-terminal region and AChBP is shown in Fig. 1. The structures of the apo and toxin-bound forms at the start of the MD simulations are shown in Fig. 2. The two starting structures superimposed very well except for the C and F loops. These loops form the toxin-binding site, and the changes are necessary to accommodate the bound toxin (21–23). The five subunits in either the apo or toxin-bound form will be referred to by their colors shown in Fig. 2; subunit-specific properties will be presented using the same color code.

The rmsds of the individual subunits from their starting conformations are shown in Fig. 3 *A* and *B* for the apo and toxin-bound forms, respectively. In the toxin-bound form, the rmsds reached stable values in ≈1 ns; the rmsds among the five subunits averaged ≈1.4 Å. In the apo form, the rmsds stabilized more slowly. For three of the subunits, with colors red, green, and blue, the rmsds also plateaued at 1.4 Å after ≈5 ns. The rmsd of the orange subunit gradually increased all of the way to the end of the 60 ns of simulations, reaching as much as 2.4 Å. The change in rmsd of the cyan subunit with time was intermediate.

The rms fluctuation (rmsf) of each subunit around its average conformation was calculated after discarding the first 5 ns of simulations (Fig. 3 *C* and *D*). Relative to the red, green, blue, and cyan subunits of the apo form, the toxin-bound form shows lower flexibilities in the C loop, the adjacent β7-β8 loop, and residues 162–167 of the F loop. The lower flexibilities of the C and F loops in the toxin-bound form most likely arise from stabilizing interactions with the bound toxin. The behavior of the orange subunit of the apo form is mixed, with high flexibility seen in residues 162–167 of the F loop (resembling the other four subunits of the apo form) but low flexibility seen in the C and β7-β8 loops (resembling the toxin-bound form).

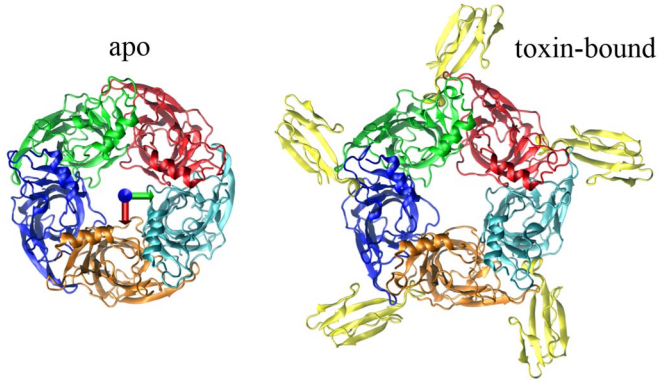

Fig. 2. Homology models of apo and toxin-bound α7 LBD, shown in top view. The five subunits are shown in different colors. Perpendicular arrows in the vestibule of the apo form indicate viewing directions.

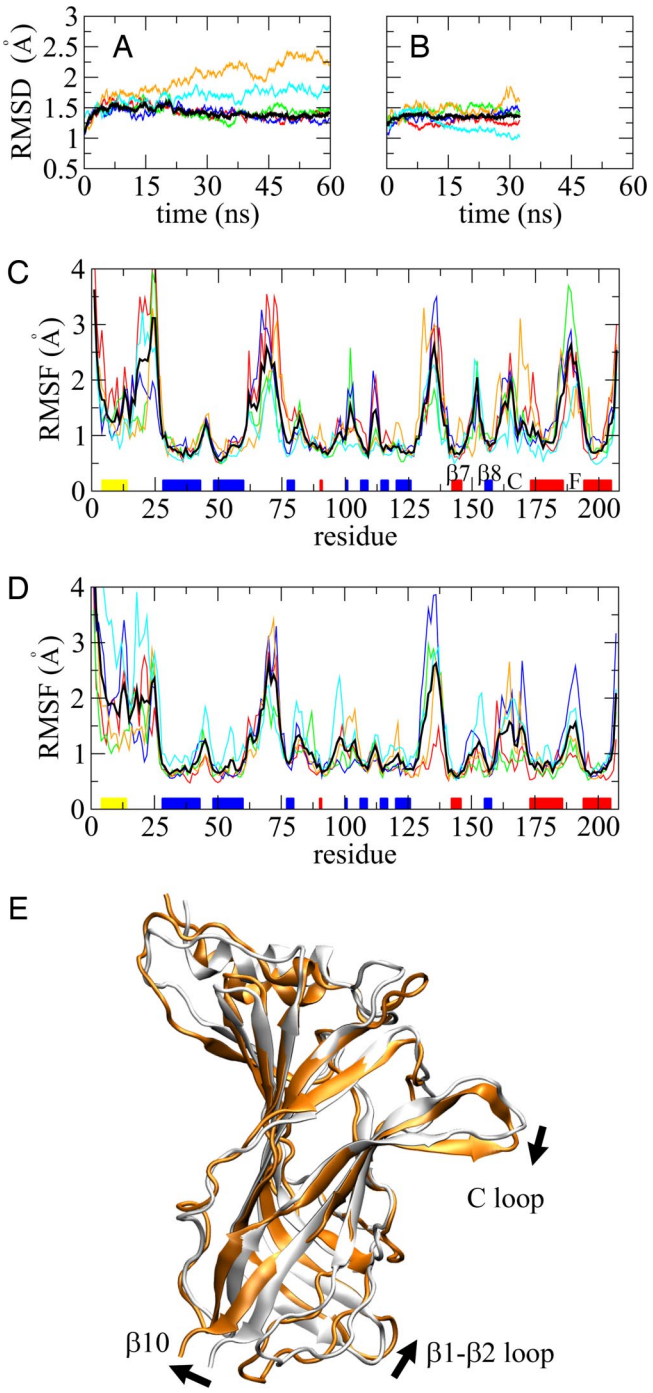

Fig. 3. Conformational change during MD simulations. (*A* and *B*) rmsds of individual subunits from their starting conformations in the apo and toxin-bound forms, respectively. In *A*, the black curve is the mean of the red, green, and blue subunits; in *B*, the black curve is the mean all of the five subunits. rmsds were calculated by using C_α atoms in β strands. (*C* and *D*) C_α rmsf in the apo and toxin-bound forms, respectively. Black curve in *C* is the mean of four subunits (excluding orange subunit); black curve in *D* is the mean of all five subunits. (*E*) Local conformational change of the apo orange subunit from the mean structure (in gray) of the red, green, and blue subunits (arrows indicate directions of relative motion). The displayed structures are the respective averages in the period of 5–30 ns along the apo trajectory.

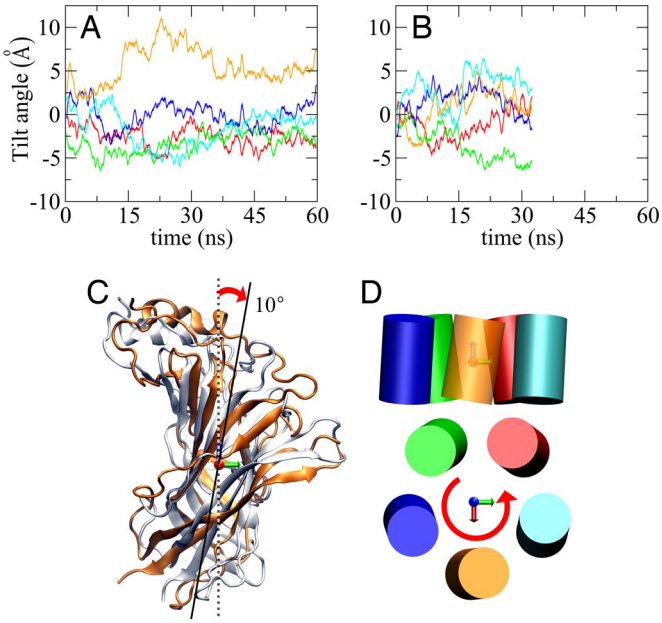

Fig. 4. Tilt of subunits along the MD trajectories. (*A* and *B*) Tilt angles in the apo and toxin-bound forms, respectively. (*C*) Tilt of the orange subunit at 22.02 ns of the apo trajectory (relative to the starting structure in gray). (*D*) Cartoon illustrating tilt of all five subunits. *Upper* and *Lower* show side and top views, respectively.

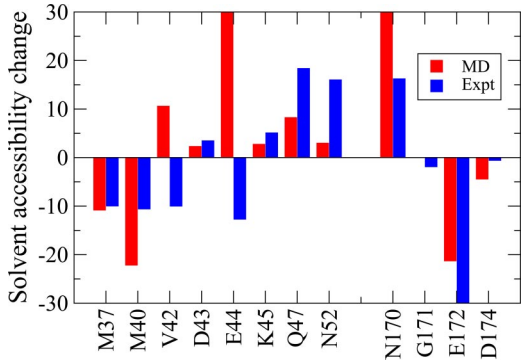

Fig. 5. Comparison in changes in solvent accessibility upon activation between MD simulations and SCAM. The MD simulation result for each residue (in Å^2) was calculated by taking the difference in solvent accessibility between the apo orange subunit and the mean of the other four subunits (averaged over the period of 15–35 ns). For residues M37 to N52, the displayed SCAM results were $-5\ln(k_M^+/k_M^-)$, where k_M^+ and k_M^- are the modification rate constants measured in the presence and absence of acetylcholine, respectively (19). For residues N170 to D174, the displayed SCAM results were the difference in percentage inhibition with and without acetylcholine (10).

The differences in rmsd and rmsf between the orange subunit and the other four subunits in the apo form prompted us to scrutinize the specific conformational change occurred in the orange subunit. In Fig. 3*E*, we compare the average structure of the orange subunit in the period of 5–30 ns with the mean structure of the red, green, and blue subunits in the same period. From a side view, the C loop and the adjacent β7-β8 loop of the orange subunit appear to swing downward and inward, whereas the F loop and the C terminus of β10 swing in the opposite direction. The β1-β2 loop swings inward (toward the vestibule). The opposite swings of the C and F loops are reminiscent of the motions seen in the targeted MD simulations of McCammon and coworkers (17). Note that in our simulations, the opposite swings occurred spontaneously, whereas in the study of McCammon and coworkers (17), the motions were triggered by pulling the C loop from the up to the down position, which was supposed to mimic agonist binding. In the cyan subunit, the C loop also moved toward the down position, but the rest of the molecule did not experience additional distortion, leading to the intermediate rmsd shown in Fig. 3*A*. The mean structure of the red, green, and blue subunits of the apo form largely resembles the mean structure of the toxin-bound form, except for the C loop, which forms part of the toxin-binding site (Fig. S2).

Tilting of Apo Orange Subunit. In addition to the local motions of the C and F loops, the apo orange subunit also exhibited rigid-body-like rotation. In general, overall rotation can be decomposed into rotations around three perpendicular axes. We set two of these to be those defining the top and side views, which are displayed as blue and red arrows in Figs. 2 and 4. Relative to the other four subunits in the apo form (Fig. 4*A*), the orange subunit developed a clockwise tilt (side view down the red axis; Fig. 4*C*). This tilt was particularly prominent in the period of 15–35 ns, reaching >10° at ≈22 ns. In comparison, none of the five toxin-bound subunits exhibited any systematic tilt (Fig. 4*B*). The tilt of the apo orange subunit follows the directions of the swings of the C and F loops. It is thus tempting to suggest that the swings of the loops triggered the tilt of the orange subunit as a whole.

If the other four apo subunits were to tilt in the same way as the orange subunit, then the LBD as a whole would appear to rotate counterclockwise when viewed from the top (Fig. 4*D*). This is the same motion seen in the first mode of normal mode analyses (14, 16, 18). We propose that the apo orange subunit is in the open conformation, with the swings of the C and F loops and concomitant tilt of the whole subunit leading to channel opening. In our simulations, only one subunit in the apo form made the excursion to the open conformation, whereas the other four subunits remained in the closed conformation. The receptor most likely becomes activated only after two or more subunits take up the open conformation (24, 25). Perhaps the probability for more than one subunit to be simultaneously in the open conformation is low, making spontaneous channel opening an infrequent event.

Experimental Evidence for Proposed Open Conformation. The agonist-induced conformational change of the LBD in the chicken α7 receptor has been probed by SCAM (10, 19). After channel activation, residues M37 and M40 on the β1 strand become more buried, but N52 on the neighboring β2 strand becomes more exposed (10). Similarly, at the tip of the F loop, residue N170 becomes more exposed, but the neighboring E172 becomes more buried (19). These opposite changes in solvent accessibilities of neighboring residues would be difficult to rationalize by models for channel activation based on rigid-body rotation alone.

However, our proposed open conformation is in broad agreement with the SCAM results, as demonstrated by the differences in residue solvent accessibility between the orange and the other four subunits. These differences, averaged over the period of 15–35 ns, are displayed in Fig. 5 for 12 residues on which SCAM data (10, 19) are available. Overall, the differences in solvent accessibility between the proposed open and closed conformations are in the same directions as the agonist-induced changes in solvent accessibility obtained by SCAM. The opposite changes in solvent accessibility between M40 and N52 and between N170 and E172 are reproduced by the open and closed conformations in our simulations. The only notable disagreement between our simulations and the SCAM data is for residues V42 and E44, located around the C terminus of β1. The solvent accessibility of these residues increased in the open conformation, but SCAM

indicated a decrease upon agonist binding. The decrease may come about because of the presence of the TMD (Fig. S1*A*), which was not included in our simulations.

The conformational change that led to the differences in solvent accessibility between the open and closed conformations, as represented by the orange subunit and the mean of the other four subunits, respectively, is illustrated in Fig. S3. In the closed conformation, residue E172 was well exposed to the vestibule, whereas N170 was partially exposed to the outside. The outward swing (i.e., away from the vestibule) of the tip of F loop in the open conformation brought E172 into the interface with the subunit in the adjacent blue, decreasing E172's solvent accessibility, and brought N170 to full exposure to the outside. The decrease in solvent accessibility of M40 in the open conformation was due to the tilt of the subunit, which brought the lower part of the subunit into closer contact with the blue subunit. Distortions in the open conformation produced the opposite changes in solvent accessibility between M37 and N52.

As further support of the proposed open conformation, the orange subunit was found to present a binding site poised for agonist binding. The C_α rmsd of the principal binding-site residues (Y92, W148, Y187, C190, and Y194) of the orange subunit and the complementary binding-site residues (W54, L108, Q116, and L118) on the adjacent cyan subunit averaged 1.5 Å over the 60-ns trajectory when compared with the corresponding residues in the carbamylcholine-bound AChBP structure [Protein Data Bank (PDB) ID code 1UV6] (21). The average rmsd increased from 1.7 to 2.2 Å when the other four subunits provided the primary binding-site residues.

Structural Validation of the LBD–Toxin Complex by Mutation Effects. As the results in Figs. 3 *B* and *D* and Fig. 4*B* indicate, relative to the apo form, the toxin-bound form was more rigid and showed a higher degree of homogeneity among the five subunits. It can thus be suggested that toxin binding locked the subunits in the closed conformation.

Changeux and coworkers (8) measured the effects of a large number of mutations on the binding affinity between the chicken α7 receptor and α-Cobratoxin. These data provided an opportunity for us to assess the structure of the LBD–toxin complex obtained from our homology modeling and MD simulations. We chose to calculate the effects of five single charge mutations that showed the highest decreases in binding affinity. Such an approach has previously allowed us to rationalize mutational effects on binding affinity and validate the structure of an ion channel–toxin complex derived from MD simulations (26–28).

Of the five chosen mutations, four (D27R, R33E, K35E, and R36E) were on the toxin, at the tip of the central loop, and one (F186E) was on the C loop of the LBD (Fig. S4*A*). The mutational effects were calculated on five snapshots from the toxin-bound trajectory between 9 and 14 ns. Although our structure lacked the TMD, this domain is distant from the toxin-binding site and hence is not expected to affect the calculation results. Overall, the mutational effects calculated on the MD structure agree well with the experimental data, although the calculation underestimated the effect of the F186E mutation (Fig. S4*B*). The agreement suggests that the structure of the LBD–toxin complex generated by the MD simulations is reasonable.

Mechanistic Model for Channel Activation and Inhibition. Changeux and Edelstein (5) have described nAChRs as allosteric proteins, in which each subunit spontaneously transitions between conformational states, and ligands (e.g., agonist, antagonist, and buffer molecules) can change a preexisting equilibrium among the conformational states. In line with this description, single-channel currents recorded by Jackson (2) demonstrated spontaneous opening of a nAChR channel, suggesting that "the acetylcholine receptor briefly and infrequently fluctuates into an active state in the absence of agonist." The spontaneous opening was inhibited by snake toxin binding. Mutational effects on spontaneous opening observed by Grosman and Auerbach (7) further indicate that "both unliganded and diliganded gating result from the same global conformational change," and that the five subunits make independent contributions to gating. Our simulations provide a glimpse into the molecular details in such a spontaneous conformational change.

By combining our MD simulations with previous experimental and computational studies, a mechanistic model for nAChR channel activation and inhibition emerges. As Fig. S5 illustrates, in the apo form, the dominant conformation of a nAChR channel is one in which each subunit as a whole is not tilted, and the C and F loops have limited interactions with neighboring subunits. Local conformational sampling of the C loop, by swinging downward and inward, and of the F loop, by swinging in the opposite direction, brings the loops into contact with their respective neighboring subunits (Fig. S5 *Right*). These initial contacts trigger the tilt of the subunit as a whole, reinforcing the intersubunit interactions. When two adjacent subunits undergo such a local-global conformational change at the same time, a binding pocket for agonists is formed at their interface. Agonist binding then locks the subunits in such an "open" conformation.

How might the conformational change within the LBD be propagated to the TMD? The C terminus of β10 is connected to the TMD M1 helix. We suggest that the up and outward motion of the C terminus of β10 seen in our simulations would pull the M1 helix and the N terminus of the M2 helix in the same direction (Fig. S1*A*). (The C terminus of the M2 helix serves as a pivot point, because it is stacked against the β1-β2 and Cys loops of the LBD.) The up and outward motion of the N terminus of the M2 helix widens the channel pore, leading to channel opening. This type of tilting motion is precisely what is implicated by recent experimental data for channel opening (11, 12).

Our model for channel activation envisions that each of the subunits can separately undergo a spontaneous conformational change, leading to intermediate states with asymmetric arrangements among the five subunits. There is indeed structural and functional evidence for asymmetry (3, 4, 7). These intermediate states perhaps provide an explanation for the existence of multiple conductance states (1, 6, 11).

The C and F loops can also swing in the reverse directions (Fig. S5 *Left*). In so doing, a binding pocket for antagonists is created. Antagonist binding locks the subunits in the closed conformation and leads to channel inhibition. The same model thus works for both activation and inhibition. Besides being supported by experimental and other computational studies noted already, this model provides a natural explanation for the observation that nAChR antagonists generally have large sizes than agonists.

Conclusion

We have explored spontaneous conformational changes of the α7 nAChR LBD by MD simulations in explicit solvent. The global and local conformational change observed in one of the subunits is consistent with previous targeted MD simulations and normal mode analyses (17, 18). That these conformational changes correspond to channel opening is supported by SCAM experiments upon agonist binding (10, 19). Our study provides atomic-scale mechanistic insight to nAChR in particular and contributes to the understanding of spontaneous conformational changes in protein function and regulation (29–31) in general.

While this article was in review, an x-ray structure of a prokaryotic pentameric ligand-gated ion channel, representing the closed conformation, was published by Hilf and Dutzler (32). Our closed conformation proposed from MD simulations is in agreement with this structure, both locally and globally (Fig. S6).

Relative to the closed conformation represented by the x-ray structure, our proposed open conformation exhibits the local and global motions highlighted above (Fig. S7). Like us, Hilf and Dutzler also suggest outward tilting of the M2 helix as the trigger for channel opening. As noted above, the motion of the C terminus of β10 seen in our MD simulation seems to play a critical role mediating between agonist binding and channel opening.

Methods

Homology Modeling. The sequence alignment and molecular modeling of the *Gallus gallus* α7 receptor LBD were performed by SWISS-MODEL (33), and the models were checked by PROCHECK (34). The hepes-bound (PDB ID code 1UX2) (21) and α-Cobratoxin bound (PDB code 1YI5) (22) structures of *Lymnaea stagnalis* acetylcholine-binding protein were selected as the templates for the α7 receptor LBD in apo and toxin-bound forms, respectively. The sequence alignment between the α7 LBD and AChBP is shown in Fig. 1. For the toxin-bound form, the five subunits of the toxin in the template (1YI5) were copied onto the homology model of the α7 LBD.

MD Simulations. The apo and toxin-bound forms were solvated in truncated octahedral periodic boxes with 17,557 water molecules and 25 sodium ions for the former, and 46,922 water molecules and 15 sodium ions for the latter. Energy minimization and MD simulations were performed by the AMBER package (35) with the modified parm99 force field (36) and TIP3P water model (37). To achieve a proper density for the systems quickly, after removing bad contacts with 2,000 steps of energy minimization, a 20-ps constant-temperature and constant-pressure (NPT) simulation (with a 0.2-ps pressure coupling time) was performed while restraining the backbone heavy atoms. Then three rounds of energy minimization (consisting of 2,000, 1,000, and 500 steps, respectively) were applied while gradually decreasing the harmonic restraining constant from 100 to 0.5 kcal/mol Å^2. Finally, the whole systems were energy-minimized for 500 steps without restraint. The MD simulations were started by gradually heating up the systems from 50 to 298 K at constant-temperature and constant-volume for 50 ps. Afterward, the simulations were switched to NPT. Nonbonded interactions were calculated with a cutoff of 9 Å, and the nonbond list was updated with a 2-Å skin width. The particle-mesh Ewald method (38) was used to treat long-range electrostatic interactions. The average temperature and pressure were maintained with a 2-ps coupling time constant at 298 K and 1 bar, respectively (39). All bonds involving hydrogen atoms were constrained with the SHAKE and RATTLE algorithms (40, 41), allowing an integration time step of 2 fs. Snapshots were saved every 10 ps for analysis. The total lengths of the MD trajectories of the apo and toxin-bound forms were 60 and 32.65 ns, respectively.

Binding Energy Calculations. Like in previous studies (26–28, 42), the electrostatic contribution to the binding free energy was calculated as

$$\Delta G_{\mathrm{el}} = G_{\mathrm{el}}\,(\text{toxin-bound}) - G_{\mathrm{el}}\,(\mathrm{LBD}) - G_{\mathrm{el}}\,(\text{toxin}), \qquad [1]$$

where G_{el} is the total electrostatic energy (Coulomb plus solvation) of a solute molecule. The effect of a charge mutation on the binding affinity was predicted as

$$\Delta\Delta G_{\mathrm{el}} = \Delta G_{\mathrm{el}}\,(\mathrm{mut}) - \Delta G_{\mathrm{el}}\,(\mathrm{WT}). \qquad [2]$$

The UHBD program (43) was used to calculate the electrostatic energy by solving the Poisson–Boltzmann equation. Each calculation started with a course grid with a 1.5-Å spacing, followed by an intermediate grid with a 0.7-Å spacing and a fine grid with a 0.25-Å spacing. The grid dimensions for all of the three spacings were 240 $\times$ 240 $\times$ 240. The first two grids were centered at the geometric center of the complex, whereas the last grid was centered at the site of mutation. Mutations were modeled onto the wild-type structure, sampled from the MD trajectory, by energy minimizing the new side chains. AMBER atomic partial charges (44) and Bondi radii (45) were used for the electrostatic calculations. The solute and solvent dielectric constants were set to 4 and 78.5, respectively, with the dielectric boundary specified by the van der Waals surface (26, 28, 42). The temperature was 298 K and ionic strength was 150 mM (with ion exclusion radius of 2 Å).

Subunit Rigid-Body Rotation. Rotation of each subunit was represented by its orientation in a global reference frame. The frame was identified with the help of a set of ''rigid'' residues, those with mean rmsfs among the five subunits $<$0.8 Å. The *z* axis of the global frame was specified as the normal to the least-squares plane of the rigid residues of the five subunits. The *x* axis lay in the plane formed by the *z* axis and the vector pointing from the center of the rigid residues of the five subunits to the center of the rigid residues of a particular subunit. Rotation angles were calculated between the global frames of a snapshot and the initial snapshot after superimposing the conformations of the subunit in these two snapshots. Rotation around the *x* axis is referred to as tilt. Note that the *z* and *x* axes define the top and side views, respectively.

ACKNOWLEDGMENTS. This work was supported in part by National Institutes of Health Grant GM058187.

1. Hamill OP, Sakmann B (1981) Multiple conductance states of single acetylcholine receptor channels in embryonic muscle cells. *Nature* 294:462–464.
2. Jackson MB (1984) Spontaneous openings of the acetylcholine-receptor channel. *Proc Natl Acad Sci USA* 81:3901–3904.
3. Unwin N, Toyoshima C, Kubalek E (1988) Arrangement of the acetylcholine receptor subunits in the resting and desensitized states, determined by cryoelectron microscopy of crystallized Torpedo postsynaptic membranes. *J Cell Biol* 107:1123–1138.
4. Villarroel A, Herlitze S, Witzemann V, Koenen M, Sakmann B (1992) Asymmetry of the rat acetylcholine receptor subunits in the narrow region of the pore. *Proc Biol Sci* 249:317–324.
5. Changeux JP, Edelstein SJ (1998) Allosteric receptors after 30 years. *Neuron* 21:959–980.
6. Zhang H, Karlin A (1998) Contribution of the beta subunit M2 segment to the ion-conducting pathway of the acetylcholine receptor. *Biochemistry* 37:7952–7964.
7. Grosman C, Auerbach A (2000) Kinetic, mechanistic, and structural aspects of unliganded gating of acetylcholine receptor channels: A single-channel study of second transmembrane segment 12′ mutants. *J Gen Physiol* 115:621–635.
8. Fruchart-Gaillard C, *et al.* (2002) Experimentally based model of a complex between a snake toxin and the alpha 7 nicotinic receptor. *Proc Natl Acad Sci USA* 99:3216–3221.
9. Henchman RH, Wang HL, Sine SM, Taylor P, McCammon JA (2003) Asymmetric structural motions of the homomeric alpha 7 nicotinic receptor ligand binding domain revealed by molecular dynamics simulation. *Biophys J* 85:3007–3018.
10. Lyford LK, Sproul AD, Eddins D, McLaughlin JT, Rosenberg RL (2003) Agonist-induced conformational changes in the extracellular domain of alpha 7 nicotinic acetylcholine receptors. *Mol Pharmacol* 64:650–658.
11. Cymes GD, Ni Y, Grosman C (2005) Probing ion-channel pores one proton at a time. *Nature* 438:975–980.
12. Paas Y, *et al.* (2005) Pore conformations and gating mechanism of a Cys-loop receptor. *Proc Natl Acad Sci USA* 102:15877–15882.
13. Law RJ, Henchman RH, McCammon JA (2005) A gating mechanism proposed from a simulation of a human alpha7 nicotinic acetylcholine receptor. *Proc Natl Acad Sci USA* 102:6813–6818.
14. Taly A, *et al.* (2005) Normal mode analysis suggests a quaternary twist model for the nicotinic receptor gating mechanism. *Biophys J* 88:3954–3965.
15. Unwin N (2005) Refined structure of the nicotinic acetylcholine receptor at 4 Å resolution. *J Mol Biol* 346:967–989.
16. Cheng X, Lu B, Grant B, Law RJ, McCammon JA (2006) Channel opening motion of alpha7 nicotinic acetylcholine receptor as suggested by normal mode analysis. *J Mol Biol* 355:310–324.
17. Cheng X, Wang H, Grant B, Sine SM, McCammon JA (2006) Targeted molecular dynamics study of C-loop closure and channel gating in nicotinic receptors. *PLoS Comput Biol* 2:1173–1184.
18. Taly A, *et al.* (2006) Implications of the quaternary twist allosteric model for the physiology and pathology of nicotinic acetylcholine receptors. *Proc Natl Acad Sci USA* 103:16965–16970.
19. McLaughlin JT, Fu J, Rosenberg RL (2007) Agonist-driven conformational changes in the inner beta-sheet of alpha7 nicotinic receptors. *Mol Pharmacol* 71:1312–1318.
20. Gao F, *et al.* (2005) Agonist-mediated conformational changes in acetylcholine-binding protein revealed by simulation and intrinsic tryptophan fluorescence. *J Biol Chem* 280:8443–8451.
21. Celie PH, *et al.* (2004) Nicotine and carbamylcholine binding to nicotinic acetylcholine receptors as studied in AChBP crystal structures. *Neuron* 41:907–914.
22. Ulens C, *et al.* (2006) Structural determinants of selective alpha-conotoxin binding to a nicotinic acetylcholine receptor homolog AChBP. *Proc Natl Acad Sci USA* 103:3615–3620.
23. Hansen SB, *et al.* (2005) Structures of Aplysia AChBP complexes with nicotinic agonists and antagonists reveal distinctive binding interfaces and conformations. *EMBO J* 24:3635–3646.
24. Sheridan RE, Lester HA (1982) Functional stoichiometry at the nicotinic receptor. The photon cross section for phase 1 corresponds to two bis-Q molecules per channel. *J Gen Physiol* 80:499–515.
25. Chang Y, Weiss DS (1999) Channel opening locks agonist onto the $GABA_C$ receptor. *Nat Neurosci* 2:219–225.
26. Dong F, Vijayakumar M, Zhou HX (2003) Comparison of calculation and experiment implicates significant electrostatic contributions to the binding stability of barnase and barstar. *Biophys J* 85:49–60.

27. Huang X, Dong F, Zhou HX (2005) Electrostatic recognition and induced fit in the κ-PVIIA toxin binding to Shaker potassium channel. *J Am Chem Soc* 127:6836–6849.
28. Dong F, Zhou HX (2006) Electrostatic contribution to the binding stability of protein–protein complexes. *Proteins* 65:87–102.
29. Kern D, Zuiderweg ER (2003) The role of dynamics in allosteric regulation. *Curr Opin Struct Biol* 13:748–757.
30. Hornak V, Okur A, Rizzo RC, Simmerling C (2006) HIV-1 protease flaps spontaneously open and reclose in molecular dynamics simulations. *Proc Natl Acad Sci USA* 103:915–920.
31. Bhattacharya N, Yi M, Zhou HX, Logan TM (2007) Backbone dynamics in an intramolecular prolylpeptide-SH3 complex from the diphtheria toxin repressor, DtxR. *J Mol Biol* 374:977–992.
32. Hilf RJC, Dutzler R (2008) X-ray structure of a prokaryotic pentameric ligand-gated ion channel. *Nature* 452:375–379.
33. Schwede T, Kopp J, Guex N, Peitsch MC (2003) SWISS-MODEL: An automated protein homology-modeling server. *Nucleic Acids Res* 31:3381–3385.
34. Laskowski RA, Macarthur MW, Moss DS, Thornton JM (1993) Procheck - A program to check the stereochemical quality of protein structures. *J Appl Cryst* 26:283–291.
35. Case DA, *et al.* (2004) AMBER 8 (Univ of California, San Francisco).
36. Simmerling C, Strockbine B, Roitberg AE (2002) All-atom structure prediction and folding simulations of a stable protein. *J Am Chem Soc* 124:11258–11259.
37. Jorgensen WL, Chandrasekhar J, Madura JD, Impey RW, Klein ML (1983) Comparison of simple potential functions for simulating liquid water. *J Chem Phys* 79:926–935.
38. Toukmaji A, Sagui C, Board J, Darden T (2000) Efficient particle-mesh Ewald based approach to fixed and induced dipolar interactions. *J Chem Phys* 113:10913–10927.
39. Berendsen HJC, Postma JPM, Vangunsteren WF, Dinola A, Haak JR (1984) Molecular-dynamics with coupling to an external bath. *J Chem Phys* 81:3684–3690.
40. Ryckaert JP, Ciccotti G, Berendsen HJC (1977) Numerical-integration of cartesian equations of motion of a system with sonstraints - Molecular-dynamics of N-alkanes. *J Comput Phys* 23:327–341.
41. Miyamoto S, Kollman PA (1992) Settle - an analytical version of the shake and rattle algorithm for rigid water models. *J Comput Chem* 13:952–962.
42. Qin S, Zhou HX (2007) Do electrostatic interactions destabilize protein-nucleic acid binding? *Biopolymers* 86:112–118.
43. Madura JD, *et al.* (1995) Electrostatics and diffusion of molecules in solution - simulations with the University-of-Houston Brownian Dynamics program. *Comput Phys Comm* 91:57–95.
44. Cornell WD, *et al.* (1996) A second generation force field for the simulation of proteins, nucleic acids, and organic molecules. *J Am Chem Soc* 117:5179–5197.
45. Bondi A (1964) Van der Waals volumes and radii. *J Phys Chem* 68:441–451.